



Role of aerosol-cloud-radiation interactions in modulating

2 summertime quasi-biweekly rainfall intensity over South China

- Hongli Chen¹, Pang-Chi Hsu¹, Anbao Zhu^{1,2}, and Xiaoyan Ma³
- 4 1State Key Laboratory of Climate System Prediction and Risk Management/Key Laboratory of Meteorological Disaster,
- 5 Ministry of Education/Collaborative Innovation Center on Forecast and Evaluation of Meteorological Disasters, Nanjing
- 6 University of Information Science and Technology, Nanjing, China
- 7 2 Joint International Research Laboratory of Atmospheric and Earth System Sciences, School of Atmospheric Sciences, Nanjing
- 8 University, Nanjing, China
- 9 3Key Laboratory for Aerosol-Cloud-Precipitation of China Meteorological Administration, School of Atmospheric Physics,
- 10 Nanjing University of Information Science and Technology, Nanjing, China
- 11 Correspondence to: Pang-Chi Hsu (pangchi@nuist.edu.cn)

Abstract. Persistent heavy rainfall events over densely populated South China are closely linked to the 12 intensification of quasi-biweekly (8–30-day) oscillations. This study examines whether and how aerosols 13 influence quasi-biweekly oscillations using observational analyses and model experiments. Statistical 14 analysis reveals a significant phase-leading relationship between increased aerosol loadings, quantified 15 by aerosol optical depth, and subsequent enhancement of 8-30-day rainfall anomalies. At the 8-30-day 16 timescale, aerosols primarily influence rainfall intensity through cloud microphysical processes, with 17 radiative effects playing a secondary role. Approximately four days before enhanced rainfall events, 18 positive aerosol anomalies contribute to increased low-level cloud water content, leading to 19 condensational latent heat release. This low-level latent heating strengthens low-level moisture 20 convergence and ascending motion, which uplifts cloud droplets above the freezing level. Subsequently, 21 additional latent heat release from mixed-phase processes (freezing/deposition) further intensifies vertical 22 motion, amplifying precipitation anomalies. Once deep convection develops, clouds absorb longwave 23 radiation, sustaining precipitation intensification. Sensitivity experiments using the Weather Research 24 and Forecasting model coupled with Chemistry (WRF-Chem) confirm these mechanisms, demonstrating 25 26 that anthropogenic aerosol enhancement intensifies precipitation anomalies through both aerosol-cloud microphysical interactions and longwave cloud-radiative effects, with the former being more dominant. 2.7 These findings highlight the need to improve aerosol-cloud microphysical parameterizations in 28 operational models to enhance the accuracy of extended-range heavy rainfall predictions in South China. 29

1





1 Introduction

Aerosols influence clouds and precipitation through two primary mechanisms: one involves directly modifying radiation, while the other acts through their role as cloud condensation nuclei (CCN) or ice nuclei (IN) (e.g., Koren et al., 2004; Tao et al., 2012; Li et al., 2015; Zhu et al., 2022; Stier et al., 2024). These are referred to as the radiative effect and the microphysical effect, respectively. The radiative effect involves the scattering and absorption of solar radiation by aerosols (i.e., the so-called "direct effect"), which leads to atmospheric heating, surface cooling, stabilization of atmospheric stratification, and suppression of precipitation (Bollasina et al., 2011). In particular, absorbing aerosols enhance cloud evaporation, thereby inhibiting cloud and precipitation formation, a phenomenon known as the semi-direct effect (Ackerman et al., 2000). The microphysical effect occurs when aerosols serve as CCN or IN (referred to as the "indirect effect"), increasing cloud droplet number concentration, enhancing cloud albedo (Twomey, 1977), reducing precipitation efficiency, and prolonging cloud lifetime (Albrecht, 1989). Additionally, the aerosol indirect effect can invigorate convective precipitation (Rosenfeld et al., 2008; Li et al., 2011; Fan et al., 2018), though its mechanisms remain poorly understood.

A recent review by Zhao et al. (2024) summarized that aerosol effects on precipitation are complex and highly variable, depending on factors such as aerosol type and concentration, precipitation characteristics and meteorological conditions, leading to substantial regional disparities. Additional uncertainties in the aerosol-precipitation relationship arise when examining different regions and timescales. While the impacts of aerosols on short-term weather phenomena (i.e., diurnal cycles and synoptic variability of rainfall) and long-term climate variations (i.e., seasonal and interannual-decadal changes in precipitation) have been well documented (e.g., Li et al., 2015; Chen et al., 2018; Sun and Zhao, 2021; Zhao et al., 2024; Chen et al., 2025), their influences on intraseasonal rainfall variability—closely linked to persistent extreme precipitation events in the Asian monsoon regions (Hsu et al., 2016; Chen et al., 2024; Xie et al., 2024) —remain poorly understood.

Prior research has primarily focused on the effects of aerosols on the intraseasonal evolution of the Indian summer monsoon; however, no consensus has yet been reached. Some studies suggest that aerosols suppress Indian monsoon rainfall (Bhattacharya et al., 2017; Dave et al., 2017; Arya et al., 2021; Surendran et al., 2022; Debnath et al., 2023), whereas others highlight their positive contribution to enhanced monsoon precipitation variations (Manoj et al., 2011; Hazra et al., 2013; Vinoj et al., 2014; Singh et al., 2019). These contrasting findings may stem from differences in datasets and models or, more fundamentally, from uncertainties in subseasonal aerosol–cloud–precipitation interactions (Li et al., 2015; Wang et al., 2022). In particular, the competing effects of radiative and microphysical processes may vary spatially and temporally, depending on aerosol type and emission sources (local vs. remote). Among these effects, the positive contribution of aerosol indirect effects on intraseasonal oscillations of the Indian





monsoon has been emphasized (Hazra et al., 2013), mainly through the enhancement of cold-rain processes involving increased ice hydrometeors and strengthened high-level latent heating.

Focusing on densely populated South China, where nonabsorbing aerosols and intraseasonal oscillations are active during the summer monsoon season (Lee et al., 2007; Huang et al., 2014; Yang et al., 2016), this study explores the role of aerosols in modulating rainfall anomalies at the quasi-biweekly (8–30-day) timescale, which is a critical factor in persistent heavy rainfall in this region (Chen et al., 2024). The relative contributions of cloud microphysical and radiative processes to rainfall intensification are examined through observational analysis and model experiments. The remainder of the paper is structured as follows. Section 2 describes the datasets and methodologies used in this study. Section 3 analyzes the observed aerosol impacts on quasi-biweekly precipitation anomalies. Section 4 presents the experimental results from the Weather Research and Forecasting model coupled with Chemistry (WRF-Chem). Concluding remarks and discussion are provided in Section 5.

2 Data and methods

2.1 Observations

Daily precipitation data were obtained from the National Oceanic and Atmospheric Administration (NOAA) Climate Prediction Center (CPC) dataset (Chen et al., 2008) with a horizontal resolution of 0.5°. Deep convection activity was analyzed using daily interpolated outgoing longwave radiation (OLR) data from NOAA at a 2.5° grid resolution (Liebmann and Smith, 1996).

Daily meteorological and aerosol data from the Modern-Era Retrospective Analysis for Research and Applications version 2 (MERRA-2), provided by the National Aeronautics and Space Administration (NASA) Global Modeling and Assimilation Office (Gelaro et al., 2017), were collected at a horizontal resolution of $0.5^{\circ} \times 0.65^{\circ}$ (longitude × latitude). Daily mean aerosol optical depth (AOD), which shows good agreement with observations (Buchard et al., 2017), was used to represent aerosol pollution conditions. Radiation variables were employed to assess the atmospheric radiative budget.

To reduce uncertainties inherent in reanalysis data, we also used the Moderate Resolution Imaging Spectroradiometer (MODIS) Collection 6 Level-3 aerosol product onboard the Terra satellite, with a horizontal resolution of 1° × 1° (Levy et al., 2013). Daily cloud parameters, including liquid cloud fraction, ice cloud fraction, cloud top pressure, cloud droplet effective radius and ice water path, were obtained from the MODIS Collection 6 Level-3 cloud product (Platnick et al., 2017). These cloud properties have been widely used to analyze aerosol indirect effects (e.g., Zhou et al., 2020; Jia et al., 2024). Additionally, three-dimensional liquid and ice cloud water content from the fifth-generation European Centre for Medium-Range Weather Forecasts (ECMWF) atmospheric reanalysis (ERA5; Hersbach et al., 2020),





with a spatial resolution of $1^{\circ} \times 1^{\circ}$ on 37 vertical levels, was collected to evaluate vertical cloud structures.

97 Specific humidity and circulation fields from ERA5 were used to conduct a moisture budget diagnostic

analysis. All datasets cover the period from 2000 to 2021, with the analysis focusing on the boreal summer

99 season (May-September, MJJAS).

2.2 Diagnostic method

To investigate the processes regulating precipitation anomalies, we diagnosed the budget equation of column-integrated moisture perturbation:

$$\langle \frac{\partial q}{\partial t} \rangle' = -\langle \mathbf{V} \cdot \nabla q \rangle' - \langle q \nabla \cdot \mathbf{V} \rangle' - \langle \frac{\partial}{\partial p} (\omega q) \rangle' - \langle \frac{Q_2}{L} \rangle', \tag{1}$$

where the primes denote the 8–30-day component derived using the Lanczos filtering method (Duchon, 1979), angle brackets indicate a mass-weighted vertical integration from 1000 to 100 hPa level, V is the horizontal wind field, q is the specific humidity, ω is vertical pressure velocity, ∇ is the horizontal gradient operator, p is pressure, L is the latent heat of condensation, and Q_2 is the apparent moisture sink as the residual of the moisture budget (Yanai et al., 1973). The terms on the right-hand side of Eq. (1) correspond to the horizontal moisture advection, moisture convergence, vertical moisture flux, and the moisture source or sink associated with phase transitions (i.e., precipitation and evaporation) at the 8–30-day timescale.

The radiative effect is quantified using MERRA-2 data. The difference between net surface radiation and net top-of-atmosphere (TOA) radiation is defined as the atmospheric net radiative change, which includes both longwave and shortwave components. Longwave and shortwave radiation can be further categorized into clear-sky radiation and cloud radiative effects. Following Lin and Chen (2023), the radiative effects driven by aerosols and greenhouse gases are isolated linearly under assumed clear-sky and/or no-aerosol conditions:

$$\begin{cases} Cld_RE = Rad - Rad_{clr} \\ GHG_RE = Rad_{clr+no_aer} \\ Aer_RE = Rad_{clr} - Rad_{clr+no_aer} \end{cases}$$
 (2)

where *Rad* represents the atmospheric net radiation flux, *Cld_RE* is the cloud radiative effect, *Aer_RE* is the aerosol radiative effect, and *GHG_RE* is the greenhouse gas radiative effect. The subscripts "*clr*" and "*clr+no_aer*" denote radiation fluxes under clear sky conditions and clear-sky/aerosol-free conditions, respectively. A positive value indicates a downward flux, contributing to atmospheric warming. Note that the *Aer_RE* in Eq. (2) captures only the direct radiative effect, as this method does not account for indirect aerosol effects on cloud properties and droplets formation (Lin and Chen, 2023).





The bootstrap method (Mudelsee et al., 2014) is applied to assess the statistical significance of results from observations and model experiments. The procedure consists of the following steps: first, paired resampled datasets are generated through random sampling with replacement from both experimental groups. Next, target statistical metrics are computed for each resampled pair. Finally, this process is repeated 1,000 times, and the 90% confidence interval is determined by selecting the 5th and 95th percentile values.

2.3 WRF-Chem experiments

The covariation of aerosols and meteorological conditions complicates the attribution of causality between aerosol–cloud–radiation interactions and precipitation in southern China through observational analyses. To address this, we conducted a series of experiments using the WRF-Chem version 4.2.2 (Grell et al., 2005; Fast et al., 2006) to verify the observed mechanisms responsible for aerosol impacts on clouds and precipitation. To increase computational efficiency, we adopted a single-domain configuration, consistent with previous studies focusing on aerosol–cloud–radiation feedbacks beyond weather timescales (e.g., Zhang et al., 2010; Chen et al., 2018). The model domain covers most of China (approximately 8°–43°N, 89°–140°E), with a horizontal resolution of 20 km and 40 vertical levels extending from the surface to 50 hPa.

The meteorological initial and boundary conditions are obtained from the National Centers for Environmental Prediction Final Analysis (NCEP-FNL) dataset, which is provided on a 1° × 1° grid and updated every six hours. Sea surface temperature (SST) data are sourced from the NCEP real-time global SST analysis. To better reproduce the observed circulation pattern, grid analysis nudging is applied to constrain meteorological variables during the spin-up period, following Yun et al. (2024).

The primary parameterization schemes used in the simulations are listed in Table 1, following the model configurations of Zhang et al. (2021). To comprehensively investigate aerosol indirect effects, the Morrison double-moment microphysics scheme (Morrison et al., 2009) and the Grell–Freitas cumulus scheme (Grell and Freitas, 2014) are employed. Shortwave and longwave radiation are parameterized using the Rapid Radiative Transfer Model for General Circulation Models (RRTMG) (Iacono et al., 2008) with aerosol radiative effects included, as the Morrison scheme enables direct communication of cloud droplet, ice, and snow effective radii to the radiation module.

Key chemistry options include the Carbon-Bond Mechanism version Z (CBMZ) scheme (Zaveri and Peters, 1999) for gas-phase chemistry, the Model for Simulating Aerosol Interactions and Chemistry (MOSAIC) 4-bin scheme (Zaveri et al., 2008) for aerosols, and the Fast-J scheme (Fast et al., 2006) for photolysis. Anthropogenic emissions are derived from the Multi-resolution Emission Inventory for China (Li et al., 2017a) and the MIX inventory (Li et al., 2017b) for regions outside China. Biogenic emissions





are calculated online using the Model of Emissions of Gases and Aerosols from Nature (MEGAN) (Guenther et al., 2012). Dust emissions are simulated using the original Goddard Chemistry Aerosol Radiation and Transport (GOCART) dust emission scheme (Ginoux et al., 2001). Biomass burning emissions are obtained from the high-resolution fire emissions dataset based on the Fire Inventory from National Center for Atmospheric Research (NCAR) version 1.5 (Wiedinmyer et al., 2011).

Table 1. Main parameterization schemes used in the WRF-Chem simulations

Option name	Schemes	References
Microphysics	Morrison double-moment	Morrison et al. (2009)
Cumulus	Grell-Freitas scheme	Grell and Freitas (2014)
Longwave radiation	RRTMG	Iacono et al. (2008)
Shortwave radiation	RRTMG	Iacono et al. (2008)
Surface layer	Monin-Obukhov	Pahlow et al. (2001)
Land surface	Unified Noah	Chen et al. (2010)
Boundary layer	Yonsei University	Hong et al. (2006)
Aerosol chemistry	MOSAIC	Zaveri et al. (2008)
Gas chemistry	CBMZ	Zaveri and Peters (1999)
Photolysis	Fast-J	Fast et al. (2006)

The case selected for simulation is a persistent heavy rainfall event over South China in July 2015, lasting over five days and characterized by high aerosol loading before the onset of heavy precipitation. To minimize uncertainties in the modeling outcomes, we perform six ensemble simulations for each experiment by perturbing the initial and boundary conditions. Specifically, the ensemble members start at one-day intervals from 4 to 9 July 2015, with all simulations ending on 6 August 2015. The first few days of each run (4–9 July) are discarded as spin-up time, and the analysis focuses on the period from 10 July to 6 August 2015.

3 Observed aerosol effects on enhanced 8-30-day rainfall anomalies

In the East Asian monsoon region, the quasi-biweekly (8–30-day) oscillation is particularly strong in southern China (18°–32°N, 108°–123°E; box in Fig. 1a) and has been identified as a key trigger of persistent heavy rainfall events (Chen et al., 2024). Meanwhile, aerosol emissions, measured by AOD, also exhibit significant quasi-biweekly variability (Fig. 1b), despite their maximum concentrations occurring in North China.





To examine whether aerosols in southern China are correlated with local extreme precipitation, we analyze the evolution of AOD (blue curve in Fig. 1c) in relation to persistent heavy rainfall events (blue bars in Fig. 1c), which are defined as daily precipitation exceeding the 90th percentile for at least three consecutive days. An increase in AOD is observed before the onset of persistent heavy rainfall, followed by a decline during the heavy rainfall period due to wet deposition. The evolution of both the heavy rainfall and AOD closely follow their respective 8–30-day components (red and purple curves in Fig. 1c), indicating that both fields are strongly modulated by the quasi-biweekly oscillation. In contrast, neither AOD nor rainfall displays quasi-biweekly variability in composites of normal rainfall cases, where amplitudes remain around the climatological mean (45th–55th percentiles). No phase-leading relationship between AOD and rainfall is observed in these cases (Fig. 1d). The distinct evolution of AOD associated with different rainfall intensities suggests that the phase-leading increase in AOD could play a role in triggering persistent heavy rainfall events, with their connections primarily manifesting at the quasi-biweekly timescale.

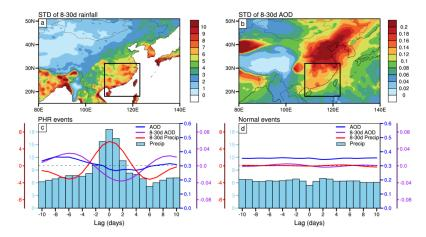


Figure 1. Spatial distributions of the standard deviation of (a) 8–30-day-filtered precipitation anomalies (mm d⁻¹) and (b) 8–30-day-filtered aerosol optical depth anomalies (AOD; unitless) during MJJAS from 2000 to 2021, based on CPC rainfall data and MERRA-2 AOD data, respectively. The black boxes indicate the study domain of southern China (18°–32°N, $108^{\circ}-123^{\circ}$ E). (c) Composites of daily precipitation (light blue bars, left *y*-axis in light blue, mm d⁻¹), 8–30-day-filtered precipitation (red curve, left *y*-axis in red, mm d⁻¹), AOD (blue curve, right *y*-axis in blue, unitless), and 8–30-day-filtered AOD (purple curve, right *y*-axis in purple, unitless) associated with persistent heavy rainfall events over South China. The *x*-axis is centered at "0", representing the median timing of individual rainfall events, with negative and positive values indicating periods before and after the event. (d) As in (c) but for the composites of normal-intensity rainfall events.

Focusing on the quasi-biweekly timescale, we further examine whether the leading phase of AOD is consistently present and essential for enhanced 8–30-day rainfall anomalies, based on statistical analyses (Fig. 2). If not, we explore under what conditions AOD contributes positively to rainfall intensification.





Based on composite analysis, starting six days before the occurrence of 8–30-day rainfall events (red curve in Fig. 2a), defined as periods with positive rainfall anomalies, AOD shows positive anomalies (blue curve in Fig. 2a). Among all 8–30-day rainfall events (249 cases), the majority (about 87%) are preceded by a leading phase of AOD anomalies, supporting a potential causal role of antecedent AOD anomalies in subsequent precipitation enhancement. Validation using multiple long-term reconstructed gridded datasets of particulate matter with aerodynamic diameter less than 2.5 micron (PM_{2.5}) confirms these findings (figure not shown), indicating that the observed leading phase of aerosols is robust, regardless of using AOD as a proxy for aerosol concentration variations. While the two AOD datasets show high consistency (blue shading in Fig. 2a), MERRA-2 AOD is used in the following observational analysis, which can capture the dynamic variations in AOD (Shi et al., 2019; Choudhury et al., 2020), since MODIS AOD is only available under cloud-free conditions.

The composite analysis in Fig. 2a illustrates the overall lead-lag phase relationship between AOD and rainfall anomalies but does not directly quantify their correlation. To further assess this correlation, Fig. 2b examines how subsequent rainfall anomalies vary with the amplitude of preceding AOD anomalies, considering all 8–30-day rainfall events. Although the correlation coefficient between the two parameters is relatively low (0.12; red line in Fig. 2b), it is statistically significant at the 90% confidence level due to the large sample size. A visual inspection suggests that this positive correlation is not well established when rainfall anomalies are weak (symbols to the left of the dashed line in Fig. 2b). However, when focusing on rainfall events with greater amplitude, the correlation becomes stronger. Specifically, for events with rainfall amplitude exceeding 0.25 standard deviation (σ) (blue line, symbols to the right of the dashed line in Fig. 2b), the correlation coefficient increases to 0.25, which is significant at the 95% confidence level. These results indicate that the effect of preceding AOD increases on subsequent rainfall enhancement is not linear.

To determine the threshold of rainfall amplitude significantly modulated by AOD magnitudes, we further compute the correlation coefficients between AOD anomalies preceding rainfall events and the amplitude of subsequent rainfall anomalies by categorizing events into different amplitude bins (x-axis in Fig. 2c). The results show that the correlation coefficient reaches 0.2, becoming significant at the 90% confidence level, when rainfall anomalies exceed the mean of all events (i.e., pink bar on the x-axis is at 0). The coefficient further increases to 0.25, surpassing the 95% confidence level, for events with rainfall amplitudes above 0.25 σ . The correlation is even stronger, reaching 0.3, for heavy rainfall events with amplitudes exceeding 1σ (rightmost pink bar in Fig. 2c). These findings suggest that higher aerosol concentrations before rainfall occurrence are conducive to rainfall amplification, particularly for events with above-average amplitude. This behavior aligns with previous studies at the synoptic and decadal



237

238239

240

241242

243

244245

246

247

248249

250

251252

253

254255

256

257

258

259

260

261

262

263

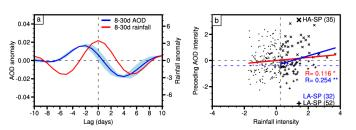
264

265

266



timescales (Wang et al., 2011; Yang et al., 2018; Shao et al., 2022; Xiao et al., 2023), which emphasize that aerosols tend to suppress light rainfall while enhancing heavy convective precipitation.



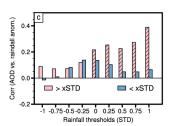


Figure 2. (a) Evolution of 8-30-day precipitation (red curve, mm d⁻¹) and 8-30-day AOD (blue curve, unitless) associated with quasi-biweekly precipitation events, defined as periods with positive 8-30-day rainfall anomalies over South China. Day 0 represents the occurrence of rainfall events, while negative and positive values on the x-axis indicate periods before and after the event. Light blue shading marks the range of one standard deviation (σ) across the two AOD datasets from MERRA-2 and MODIS. (b) Scatterplot of rainfall intensity (i.e., 8-30-day-filtered rainfall anomalies at Day 0; x-axis, mm d-1) versus preceding AOD intensity (represented by the peak value of 8-30-day-filtered AOD anomalies during Days -6 to -1; y-axis, unitless), with both variables normalized by their climatology. The red line represents the linear regression fitted to all cases, while the blue line corresponds to events where rainfall intensity exceeds 0.25\u03c3. The correlation coefficients between the two variables are shown in the bottom right corner, with single and double asterisks indicating significance at the 90% and 95% confidence levels, respectively. Enhanced 8-30-day rainfall events (>0.25σ) are classified into High AOD-Strong Precipitation (HA-SP; cross sign) and Low AOD-Strong Precipitation (LA-SP; plus sign) categories, with case counts displayed in each quadrant. To maintain nearly equal sample sizes for these two groups, the LA-SP classification is determined using an AOD anomaly threshold of -0.4σ (blue dashed line and blue text). (c) Correlation coefficients between preceding AOD intensity and rainfall intensity at Day 0 for different rainfall amplitude thresholds (bins with 0.255 intervals). Pink bars represent correlations when 8-30-day rainfall exceeds a given threshold, while blue bars show correlation coefficients for the remaining events. Hatching indicates correlations significant at the 90% confidence level.

The statistical results in Fig. 2 indicate that AOD anomalies have a more pronounced impact on 8–30-day precipitation events exceeding a certain intensity threshold (e.g., 0.25σ), with stronger antecedent AOD anomalies leading to amplified subsequent precipitation anomalies. To investigate the physical processes through which AOD contributes to rainfall intensification, we compared enhanced 8–30-day rainfall cases (amplitude greater than 0.25σ) under varying AOD intensities prior to the event, categorized as High AOD–Strong Precipitation (HA–SP) and Low AOD–Strong Precipitation (LA–SP) cases. Thus, preceding AOD cases are classified as high or low based on whether the standardized AOD anomaly is positive or negative. To ensure balanced sample sizes, LA–SP cases with AOD anomalies between 0 and –0.4σ were excluded (Fig. 2b).

Composite patterns of convection and circulation during the early and peak phases of HA-SP and LA-SP events, along with their differences, are shown in Fig. 3. At four days before the occurrence of





heavy rainfall events (Day –4), both types of events exhibit suppressed convection of similar magnitude but with distinct wind anomalies (contours and vectors in Figs. 3a, d, g), which likely explain their differing AOD behaviors. HA–SP events are associated with anomalous northerlies that transport aerosols from North China to South China, increasing regional AOD, whereas LA–SP events exhibit an opposite transport pattern. Moreover, the anomalous moisture convergence (vectors in Fig. 3g) coincides with significant AOD enhancement (shading in Fig. 3g) and intensified convection over coastal Southern China (contours in Fig. 3g), implying the aerosol effects on moistening process. Approximately two days before the heavy rainfall events, convective anomalies (indicated by negative OLR anomalies) were observed over South China in both cases (contours in Figs. 3b, e). However, in high AOD cases (HA–SP), convection and moisture convergence signals are noticeably stronger than in low AOD cases (LA–SP) (Fig. 3h). At the peak of the heavy rainfall event (Day 0), strong convection, cyclonic circulation anomalies, and significant moisture convergence dominate South China (Figs. 3c, f), coinciding with AOD reductions due to wet scavenging. Notably, convective anomalies at Day 0 are more intense in HA–SP events than in LA–SP events (Fig. 3i), suggesting that preceding positive AOD anomalies may amplify subsequent convective activity through enhanced moisture convergence.

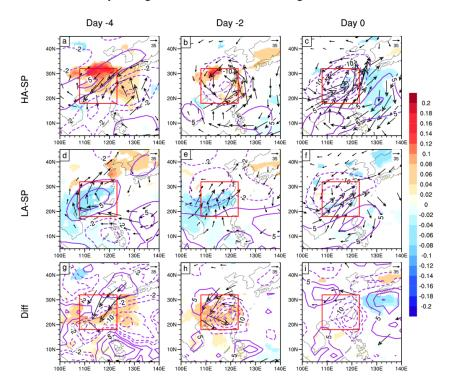


Figure 3. (a)–(c) Composite evolution of 8–30-day outgoing longwave radiation (OLR; purple contours, W m⁻²), AOD (shading, unitless), and column-integrated moisture flux (vectors, kg m⁻¹ s⁻¹) at 4, 2, and 0 days before the occurrence of HA–SP events, respectively. (d)–(f) and (g)–(i) Similar to (a)–(c), but for the composite results of LA–SP events and



287

288

289

290

291

292

293

294

295

296297

298

299

300

301

302

303

304305

306

307 308

309

310

311312

313

314

315

316



the differences between HA-SP and LA-SP events, respectively. Only AOD and moisture flux anomalies with statistically significant changes at the 90% confidence level are shown. The red box outlines the study domain of South China.

Based on the moisture budget diagnosis, we further examine the processes responsible for increasing moisture and enhancing rainfall amplitude in HA–SP cases, comparing the budget terms with those in LA–SP events (Figs. 4a–c). In both cases, moisture convergence ($-\langle q\nabla \cdot V\rangle'$, green curves in Figs. 4a–b) serves as the primary moisture source, also accounting for the differences in rainfall amplitude between HA–SP and LA–SP events (green curve in Fig. 4c). The moisture sink associated with latent heating is in phase with rainfall and offsets the moisture source from convergence. Nevertheless, their combined effect still contributes positively to heavy rainfall occurrence. The temporal evolution of these key terms reveals their sequential influence. The increase in AOD slightly precedes the enhancement of moisture convergence (blue and green curves in Fig. 4c), indicating that the aerosols could play roles in moistening process, which may subsequently lead to intensified rainfall (red curve in Fig. 4c). Other moisture processes have relatively minor contributions, and their differences between HA–SP and LA–SP events are not statistically significant.

Building on the observed lead-lag relationship between aerosols and moistening process (Figs. 4ac), the next question is: through what physical processes do aerosols enhance moisture convergence and rainfall? Previous studies have shown that aerosols primarily influence summer precipitation in South China through cloud microphysical effects, as clouds in this region are readily invigorated by the aerosols which are less absorbing and highly hygroscopic (Fan et al., 2008; Yang et al., 2016). To investigate this mechanism, we analyzed several key cloud-related parameters for HA-SP and LA-SP events (Figs. 4df). Although the temporal evolution of cloud properties is similar in both cases (Figs. 4d-e), their magnitudes exhibit notable differences (Fig. 4f). The most significant increase prior to heavy rainfall in HA-SP events is observed in the ice water path (orange curve in Fig. 4f), following an increase in liquid cloud fraction (purple curve in Fig. 4f). These changes are likely linked to precursor moisture convergence anomalies (green curve in Fig. 4c), which enhance latent heating in the lower troposphere. The resulting low-level warming destabilizes atmospheric stratification, facilitating the uplift of abundant cloud droplets above the freezing level. Consequently, the ice water path increases markedly (orange curve in Fig. 4f), while the modest and insignificant increase in ice cloud fraction may reflect a limited reduction in the liquid cloud fraction and persistent supercooled droplets. These conditions favor interactions between supercooled droplets and cloud ice.



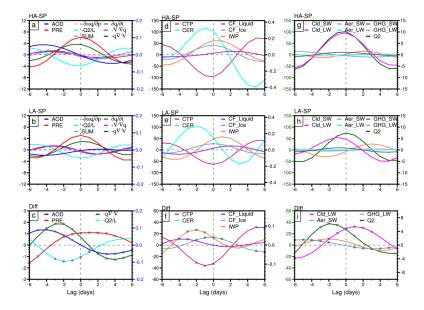


Figure 4. As in Fig. 2a, but for the composite evolution of 8–30-day (a) precipitation (red curve; left *y*-axis, mm d⁻¹), AOD (blue curve; right *y*-axis in blue, unitless), and individual moisture budget terms (various colored curves representing each budget term in Eq. (1); left *y*-axis, mm d⁻¹) associated with HA–SP events. (d, g) As in (a), except that (d) shows the 8–30-day evolution of cloud top pressure (CTP; magenta curve; left *y*-axis, hPa), ice water path (IWP; orange curve; left *y*-axis, g m⁻²), cloud droplet effective radius (CER; orange curve; right *y*-axis, μm), liquid cloud fraction (CF_Liquid; purple curve; right *y*-axis, unitless), and ice cloud fraction (CF_Ice; light blue curve; right *y*-axis). Panel (g) presents 8–30-day column-integrated latent heat heating (*Q*₂; green curve; left *y*-axis in green, W m⁻²) and 8–30-day radiative budget terms calculated from Eq. (2) (right *y*-axis, W m⁻²), including longwave/shortwave cloud radiative effects (Cld_LW/Cld_SW; magenta curve/pink curve), longwave/shortwave aerosol direct radiative effects (Aer_LW/Aer_SW; cyan curve/light blue curve), and longwave/shortwave greenhouse gas radiative effects (GHG_LW/GHG_SW; orange curve/gray curve). (b, e, h) and (c, f, i) are similar to (a, d, g), but represent the composite results for LA–SP events and the differences between HA–SP and LA–SP events, respectively. In panels (c) and (i), only terms with statistically significant differences at the 90% confidence level are shown, with significant periods marked by gray asterisks.

Subsequently, deep convective clouds develop, characterized by a reduction in cloud top pressure (magenta curve in Fig. 4f) and an increase in ice cloud fraction (light blue curve in Fig. 4f), alongside a gradual weakening of the liquid cloud fraction (purple curve in Fig. 4f). Additional latent heat released from freezing and deposition could further enhance upward motion, collectively amplifying the intensity of 8–30-day heavy precipitation events. Note that both cases exhibit positive anomalies in the effective radius of cloud droplets before the onset of heavy precipitation (cyan curves in Figs. 4d–e), although the difference between them is not statistically significant. This suggests that aerosol impacts on the warm-rain processes are not the primary driver of the 8–30-day rainfall enhancement, with aerosol indirect effects likely exerted through ice-phase microphysical processes.





In addition to aerosol–cloud interactions, changes in liquid and ice cloud fractions also influence atmospheric radiation variations. The right panels of Fig. 4 illustrate the longwave and shortwave radiative effects induced by clouds, aerosols, and greenhouse gases. During HA—SP events, the dominant longwave cloud-radiative effect closely follows the temporal evolution of 8–30-day precipitation anomalies (magenta curve in Fig. 4g), supporting the maintenance of heavy precipitation intensity (Chen et al., 2024). Although the amplitude is relatively small, the significant increase in GHG-induced longwave heating prior to heavy rainfall (orange curve in Fig. 4i) may be associated with the preceding phase of moistening driven by moisture convergence anomalies (green curve in Fig. 4c). Focusing on the aerosol effect, the aerosol-induced direct shortwave atmospheric heating (light blue curve in Fig. 4i) is small but in phase with AOD anomalies (blue curve in Fig. 4c). This suggests that some absorbing aerosols, such as anthropogenic black carbon, may contribute to shortwave radiation absorption over southern China. However, due to the predominance of nonabsorbing aerosols in this region (Lee et al., 2007; Huang et al., 2014; Yang et al., 2016), the resultant aerosol shortwave radiative forcing (Aer_SW) remains relatively weak (light blue curve in Fig. 4i).

Both the aerosol-induced direct radiative effects (light blue curve in Fig. 4i) and longwave cloud-radiative effects (magenta curve in Fig. 4i), with magnitudes of approximately 2–5 W m⁻², are significantly smaller than atmospheric latent heating associated with moisture processes, which exceeds 30 W m⁻² (green curve in Fig. 4i). This indicates that aerosol–cloud microphysical effect plays a dominant role in enhancing heavy precipitation at the 8–30-day timescale, as demonstrated by the diagnostic frameworks of moisture and radiative budget analyses.

To confirm the stepwise contribution of aerosol-induced low-level moistening to high-level freezing and deposition, ultimately leading to deep convection and rainfall intensification, as discussed in Fig. 4, we further analyze the time-height evolution of latent heating, vertical velocity, and liquid/ice cloud water content differences between HA-SP and LA-SP events (Fig. 5). As shown in Fig. 5a, low-level liquid cloud water content increases below 500 hPa, coinciding with peak AOD at four days (Day -4) before the occurrence of heavy rainfall events (Fig. 4). The condensation process in shallow convection releases latent heat, forming a positive latent heating anomaly centered at 850 hPa (Fig. 5c), which enhances low-level moisture convergence and upward motion (Fig. 5d). This process provides favorable conditions for the uplift of cloud droplets above the freezing level. From Days -3 to -1, strong latent heating (Fig. 5c) and ascending motion anomalies (Fig. 5d) develop above 500 hPa, corresponding to the maxima of ice cloud water content in the middle and upper troposphere (Fig. 5b). The intensified conversion of supercooled cloud water to ice hydrometeors through freezing and deposition further releases latent heat, reinforcing vertical motion and convection. Ultimately, these processes lead to the intensification of rainfall anomalies.





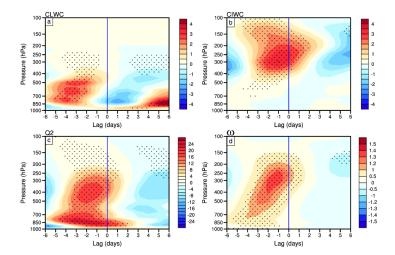
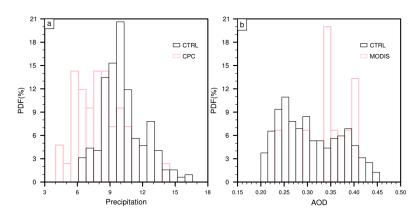


Figure 5. Height–time evolution of 8–30-day anomalies in (a) liquid cloud water content (CLWC; 10^{-6} kg kg⁻¹), (b) ice cloud water content (CIWC; 10^{-6} kg kg⁻¹), (c) latent heat heating (J kg⁻¹ h⁻¹), and (d) vertical velocity anomalies (-10^{-2} Pa s⁻¹) between the HA–SP and LA–SP events. Stippling denotes differences statistically significant at the 90% confidence level. Vertical blue lines denote the timing of heavy rainfall event occurrence (Day 0).

4 Verification of mechanisms using WRF-Chem experiments

Due to the complex interactions between aerosols and rainfall, as well as the limited availability of observational data on cloud microphysical properties, we employ the WRF-Chem model to verify the mechanisms identified in Sect. 3. Following the methodology of Guo et al. (2022) and Yun et al. (2024), we conduct two sets of simulations to assess the effects of anthropogenic aerosols. In the control experiment (CTRL), anthropogenic aerosol emissions are kept unchanged, while in the sensitivity experiment (CLEAN), emissions are scaled to 10% of those in the CTRL run. Hence, we examine differences in cloud microphysics, radiation, and surface rain rates between the CTRL and CLEAN simulations.







© BY

Figure 6. Probability density functions (PDFs) of (a) daily precipitation (mm d^{-1}) and (b) AOD (unitless) from observations (pink curves, CPC rainfall and MODIS AOD data) and the CTRL experiment (black curves) during the model integration period over the key region of interest ($21^{\circ}-24^{\circ}N$, $111^{\circ}-116^{\circ}E$) in South China.

Before conducting sensitivity experiments, we evaluate the reliability of the model simulations by comparing the probability density functions of precipitation and AOD from the CTRL experiment with observations over the key region of South China (21°–24°N, 111°–116°E), where the primary 8–30-day heavy precipitation event occurred in July 2015 (Fig. 6). The precipitation distribution from the CTRL simulation (black bars in Fig. 6a) generally resembles the observed distribution (pink bars in Fig. 6a), although it tends to slightly overestimate precipitation intensity. This bias is common in regional climate models, including WRF, and is attributable to limitations in convective cloud and microphysical parameterizations (Caldwell et al., 2009; Argüeso et al., 2012). Additionally, the CTRL simulation captures the overall pattern of the observed AOD distribution, though the simulated peaks are underestimated (Fig. 6b). This discrepancy is likely due to uncertainties in emission inventories and biases in meteorological fields (Huang and Ding, 2021). Despite these biases, the CTRL experiment demonstrates reasonable skill in reproducing the observed precipitation and AOD distributions over the study area.

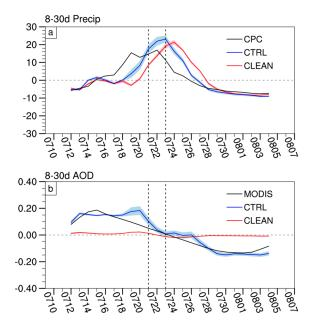


Figure 7. Evolution of (a) precipitation (mm d^{-1}) and (b) AOD (unitless) anomalies averaged over the Pearl River Delta (21°–24°N, 111°–116°E) in the observations (black curves, CPC rainfall and MODIS AOD data), CTRL (blue curves) and CLEAN (red curves) experiments. Colored shading represents the range of 0.5 σ across the six ensemble members.





By comparing rainfall and AOD anomalies—both subjected to a 5-day running mean to remove high-frequency synoptic signals and focus on the subseasonal timescale—between the CTRL and CLEAN experiments, the observed relationship between preceding AOD and heavy rainfall is confirmed (Fig. 7). Notably, the CTRL experiment captures the temporal evolution of precipitation and AOD anomalies reasonably well, despite slight biases in the timing of their peaks. An increase in AOD precedes the intensification of rainfall (blue curves in Figs. 7a–b), consistent with the observations (black curves in Figs. 7a–b). This further supports the reliability of the model simulations employed in this study. When AOD is suppressed in the CLEAN experiment, rainfall amplitude decreases accordingly (red curves in Figs. 7a–b). The most significant reduction in rainfall amplitude occurs when AOD declines notably between 21–23 July, which will be the focus of the following analyses.

To verify whether aerosols drive rainfall intensification through the aerosol-cloud interactions identified in Sect. 3, we compare these cloud-related variables between the CTRL and CLEAN simulations (Fig. 8). When aerosols are enhanced (transition from CLEAN to CTRL), the key region exhibits an increase in column cloud fraction (Fig. 8a), with distinct positive anomaly centers in the lower troposphere (925 hPa) and upper troposphere (200 hPa). The increase in low-level cloud fraction is attributed to aerosol-induced enhancement in cloud droplet number concentration (figure not shown) and liquid cloud water content (Fig. 8b). Between 700–400 hPa, higher supersaturation promotes increased cloud water formation (Fig. 8b), consistent with observational findings (Fig. 5b). The enhanced upper-level cloud fraction is associated with an increase in ice-phase hydrometeors (Figs. 8d–f), where cloud ice likely forms through cloud water freezing and vapor deposition. Meanwhile, snow growth appears to be driven by depositional processes and the riming of abundant cloud droplets. Although graupel mixing ratios also increase, their magnitude is much smaller compared to the dominant snow mixing ratios. Overall, cold-phase and mixed-phase processes amplify atmospheric rain mixing ratios (Fig. 8c), confirming the observed aerosol-mediated precipitation intensification through enhanced cloud water and cloud ice pathways (Figs. 4–5).

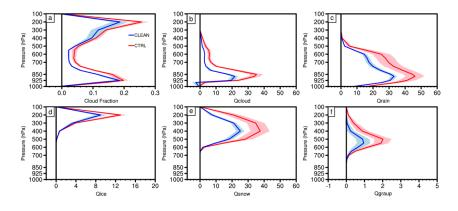






Figure 8. Vertical profiles of (a) cloud fraction anomalies (unitless) and (b)–(f) hydrometeor mixing ratio anomalies (10^{-6} kg kg⁻¹) averaged over the key region for the CTRL and CLEAN experiments during 21–23 July 2015: (b) cloud water anomalies, (c) raindrop anomalies, (d) cloud ice anomalies, (e) snow anomalies, and (f) graupel anomalies. Colored shading represents $\pm 0.5\sigma$ across the six ensemble members.

To examine the stepwise modulation of heavy rainfall occurrence by aerosol-induced low-level moistening and deep convection development, we compare the vertical profiles of latent heating anomalies, vertical velocity anomalies, and moisture convergence anomalies between the CTRL and CLEAN simulations (Figs. 9a–c). When aerosols are enhanced, the increased latent heating rate exhibits two distinct centers at 850 hPa and 400 hPa (Fig. 9a), consistent with observed profiles (Fig. 5a). These heating centers correspond to enhanced low-level cloud water and increased high-level cloud ice and snow concentrations (Fig. 8), where latent heat is released through condensation at lower levels and freezing and riming processes at upper levels. Thus, aerosols intensify latent heating through cold-phase and mixed-phase processes, strengthening upward motion throughout the atmosphere (Fig. 9b), similar to the observed patterns (Fig. 5c). Simultaneously, aerosol-induced enhanced low-level moisture convergence anomalies (Fig. 9c) further increase supersaturation and latent heating, amplifying the intensity of rainfall anomalies.

Based on observational diagnostics, we suspect that aerosol-cloud microphysical processes contribute more significantly to rainfall intensification than aerosol-cloud radiative effects (Fig. 5i). To verify this, we analyze the vertical profiles of longwave radiative heating anomalies (Fig. 9d) in the CTRL and CLEAN experiments, along with changes in longwave and shortwave radiation fluxes (Figs. 9e-f). In the CTRL experiment, longwave radiative heating exhibits minimal changes below 925 hPa but generally increases between 850–500 hPa and above 400 hPa (Fig. 9d), consistent with the vertical profile of enhanced cloud fractions (Fig. 8a). To quantify cloud contributions to atmospheric longwave heating, we calculate the longwave cloud-radiative effect using all-sky and clear-sky radiative fluxes based on Eq. (2) (gray bars in Fig. 9e). The development of deep convection triggered by enhanced aerosol emissions reduces OLR at the TOA while increasing atmospheric longwave radiation and downward longwave radiation at the surface. For shortwave radiation, the increased cloud cover reflects more shortwave radiation back to the TOA (gray bars in Fig. 9f). Additionally, the dominance of scattering aerosols (e.g., sulfate aerosols) during this rainfall event contributes to a small shortwave radiation flux (blue bars in Fig. 9f).

These modeling results align with observations, showing that latent heating rates are stronger than radiative heating rates (Figs. 9a, d). This suggests that aerosol-driven cloud microphysical processes dominate the total heating contribution, while radiative processes play a secondary role (Fig. 4). The main conclusions remained robust in high-resolution simulations with two nested domains (figure not shown).





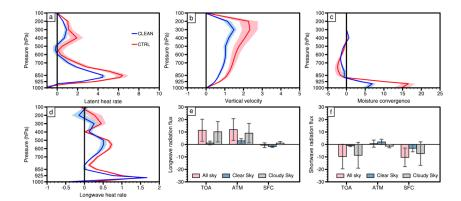


Figure 9. As in Fig. 8, but for the vertical profiles of (a) latent heat flux anomalies (K d⁻¹), (b) vertical velocity anomalies (m s⁻¹), (c) moisture convergence anomalies (10^{-2} kg kg⁻¹ s⁻¹), and (d) longwave radiative heating rate anomalies (K d⁻¹) in the CTRL and CLEAN experiments. (e) Anomalous longwave radiation fluxes (W m⁻²) averaged over the key region at the top of the atmosphere (TOA), within the whole atmosphere (ATM), and at the surface (SFC) under all-sky (pink bars), clear-sky (blue bars), and cloudy-sky (gray bars) conditions. (f) Similar to (e), but for anomalous shortwave radiative fluxes. Colored bars represent the ensemble mean from six simulations, while whiskers indicate the range of $\pm 0.5\sigma$ across the six ensemble members.

5 Summary and discussion

South China, a densely populated region, frequently experiences persistent heavy rainfall events that are closely linked to 8–30-day rainfall anomalies. This study investigates how anthropogenic aerosols intensify these quasi-biweekly rainfall anomalies using observational diagnostics and model simulations. Statistical analysis reveals that aerosol concentrations tend to increase approximately four days before the occurrence of rainfall anomalies. The phase-leading increase in AOD is positively correlated with subsequent rainfall intensity, primarily by enhancing moisture convergence, which strengthens deep convection and precipitation. The evolution of moisture sources, cloud properties, and radiative processes suggests that aerosol–cloud microphysical effects play a dominant role in rainfall enhancement, while radiative feedbacks have a secondary influence. These processes are summarized in Fig. 10.

For aerosol-cloud microphysical effects (red and pink sectors in Fig. 10), increased aerosol concentrations enhance CCN activation, promoting the accumulation of low-level cloud water. Latent heat release from the condensation of low-level cloud water induces localized warming, which reduces surface pressure anomalies, strengthens upward motion, and enhances moisture convergence. This facilitates the uplift of cloud droplets above the freezing level, where additional latent heat release from cold-phase and mixed-phase processes (freezing and deposition) further amplifies ascending motion, leading to stronger deep convection and intensified rainfall anomalies. In addition to microphysical effects, aerosols in southern China can absorb shortwave radiation, while aerosol-induced changes in water vapor





and cloud cover also contribute to increased longwave radiation. These radiative processes are illustrated on the right side of Fig. 10 (blue and light blue sectors). The resulting radiative heating provides additional energy for deep convection and enhances moisture flux, further supporting rainfall development.

WRF-Chem experiments for a heavy rainfall event in July 2015, conducted under different aerosol emission conditions, confirm the observational findings. Under CLEAN conditions, where anthropogenic aerosol concentrations are greatly reduced, precipitation anomalies weaken due to suppressed cold-phase and mixed-phase processes. In contrast, in the CTRL experiment, increased aerosols appear before enhanced rainfall occurrence, consistent with observations. Enhanced low-level cloud water and mid-to-upper-level ice hydrometeors lead to the formation of dual latent heating centers at 850 hPa and 400 hPa, which drive stronger low-level moisture convergence and column-wide upward motion, ultimately intensifying precipitation anomalies. While longwave cloud-radiative effects marginally increase atmospheric moist static energy, their contribution to precipitation anomalies is relatively weaker. These modeling results further corroborate the aerosol-driven intensification of quasi-biweekly precipitation observed in South China.

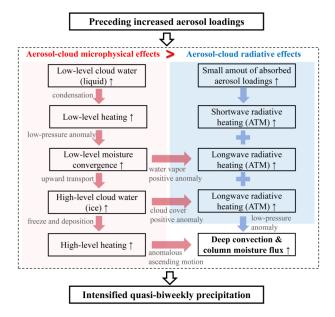


Figure 10. Schematic diagram illustrating the mechanisms of aerosol effects on heavy rainfall events at the 8–30-day timescale. The symbol "↑" denotes the enhancement of the corresponding processes, "ATM" refers to the whole atmosphere, and ">" indicates stronger contributions of the process to heavy precipitation events.

Numerous studies on synoptic and long-term aerosol effects have reported that cloud liquid accumulated by aerosols is converted into ice hydrometeors above the freezing level, thereby invigorating deep convection and intensifying heavy precipitation, the so-called invigoration effect (e.g., Rosenfeld et al., 2008; Li et al., 2011; Hazra et al., 2013; Guo et al., 2014). Aligning with this framework, our





observational analysis shows that aerosols similarly enhance cold-phase and mixed-phase cloud development at the 8-30-day timescale, leading to further intensification of heavy precipitation. Our findings contribute to a deeper mechanistic understanding of aerosol-cloud-radiation interactions in modulating precipitation anomalies at the intraseasonal timescale over southern China. Note that the positive contribution of increased AOD to rainfall intensification contrasts with previous studies on the Indian summer monsoon, which reported a link between increased 20-100-day-filtered AOD and the intensification of monsoon breaks (Arya et al., 2021; Surendran et al., 2022). This discrepancy may be attributed to differences in aerosol types and concentrations between the two monsoon regions. In the Indian monsoon region, rainfall suppression has been associated with the indirect effect of dust aerosols through reduced cloud effective radius and decreased precipitation efficiency, whereas nonabsorbing aerosols are more prevalent in southern China (Lee et al., 2007; Huang et al., 2014). Furthermore, Singh et al. (2019) showed that a simultaneous enhancement of dust emissions from West Asia and the Tibetan Plateau intensify the Indian monsoon rainfall with 10–20-day periodicity, but remarkably decrease the spatial scale of the 30-60-day rainfall. Hence, it would be valuable to investigate whether aerosol impacts vary across intraseasonal timescales in southern China, such as the 8-30-day and 20-100-day bands, which we leave for future study.

Given that intraseasonal variability serves as a key source of subseasonal predictability for extreme events (e.g., Wei et al., 2024; Xie et al., 2024), which remains a challenge for both the scientific and operational communities, these results provide valuable insights for improving subseasonal prediction skill by refining aerosol–cloud microphysical processes in prediction models. However, the extent to which aerosols influence subseasonal prediction skill for extreme events requires further investigation. Modulated by intraseasonal convective and circulation anomalies, aerosols exhibit significant variability at the subseasonal timescale (e.g., Tian et al., 2011; Reid et al., 2015; Yu and Ginoux, 2021). However, the factors controlling aerosol loading at the quasi-biweekly timescale in South China remain an open question. At this timescale, the quantitative contributions of aerosol–radiation and aerosol–cloud interactions to heavy rainfall events also warrant further in-depth exploration (e.g., Liu et al., 2020; Zhang et al., 2021). These aspects are the focus of our ongoing research.

Data Availability. The source codes of the WRF-Chem model are available on the University Corporation for Atmospheric Research (UCAR) website at https://www2.mmm.ucar.edu/wrf/users/download/get_source.html (UCAR, 2025a). The FNL data are available at https://rda.ucar.edu/datasets/ds083.2/ (NCEP, NWS, NOAA, U.S. DOC, 2000). The biomass burning emission data of FINN version 1.5 can be obtained at https://www.acom.ucar.edu/Data/fire/(UCAR, 2025b). The MEIC and MIX anthropogenic emissions are available at http://meicmodel.org.cn/



581



University, CEADs, CAEP, ERA5 data available 552 (Tsinghua 2025). The are 27 https://cds.climate.copernicus.eu/datasets April 2025), (last access: 553 https://doi.org/10.24381/cds.bd0915c6 (Hersbach et 2023). MERRA-2 554 al., reanalysis data (https://doi.org/10.5067/Q9QMY5PBNV1T, GMAO, 2015a) aerosol and data 555 (https://doi.org/10.5067/KLICLTZ8EM9D, GMAO, 2015b) available 556 are at https://disc.gsfc.nasa.gov/datasets (last access: 27 April 2025). The MODIS data is available at 557 https://doi.org/10.5067/MODIS/MOD08 D3.061 (Platnick et al., 2015). The CPC precipitation and OLR 558 data are openly available from NOAA at https://psl.noaa.gov/data/gridded/data.cpc.globalprecip.html 559 (NOAA, 2025a) and https://psl.noaa.gov/data/gridded/data.olrcdr.interp.html (NOAA, 2025b), 560 respectively. 561 562 Author contributions. PCH and HC conceptualized the research goals and aims. HC performed the 563 analysis and wrote the manuscript draft. AZ and HC ran the simulations. PCH, AZ, and XM reviewed 564 and edited the manuscript. 565 566 Competing interests. The contact author has declared that none of the authors has any competing 567 interests. 568 569 Acknowledgments. This work was supported by the National Natural Science Foundation of China 570 (42225502). We acknowledge the High Performance Computing Center of Nanjing University of 571 Information Science and Technology for their support of this study. We also thank all the corresponding 572 institutions for providing their data for this study. 573 574 575 Financial support. This research has been supported by the National Natural Science Foundation of China (42225502). 576 References 577 Ackerman, A. S., Toon, O. B., Stevens, D. E., Heymsfield, A. J., Ramanathan, V., and Welton, E. J.: Reduction of 578 Tropical Cloudiness by Soot, Science, 288, 1042-1047, https://doi.org/10.1126/science.288.5468.1042, 2000. 579

Albrecht, B. A.: Aerosols, Cloud Microphysics, and Fractional Cloudiness, Science, 245, 1227-1230,

https://doi.org/10.1126/science.245.4923.1227, 1989.





- 582 Argüeso, D., Hidalgo-Muñoz, J. M., Gámiz-Fortis, S. R., Esteban-Parra, M. J., and Castro-Díez, Y.: High-resolution
- 583 projections of mean and extreme precipitation over Spain using the WRF model (2070–2099 versus 1970–1999), J.
- Geophys. Res.-Atmos., 117, https://doi.org/10.1029/2011JD017399, 2012.
- 585 Arya, V. B., Surendran, S., and Rajendran, K.: On the build-up of dust aerosols and possible indirect effect during Indian
- 586 summer monsoon break spells using recent satellite observations of aerosols and cloud properties, J. Earth Syst. Sci.,
- 587 130, 42, https://doi.org/10.1007/s12040-020-01526-6, 2021.
- 588 Bhattacharya, A., Chakraborty, A., and Venugopal, V.: Role of aerosols in modulating cloud properties during active-
- 589 break cycle of Indian summer monsoon, Clim. Dynam., 49, 2131-2145, https://doi.org/10.1007/s00382-016-3437-
- 590 4, 2017.
- 591 Bollasina, M. A., Ming, Y., and Ramaswamy, V.: Anthropogenic Aerosols and the Weakening of the South Asian
- 592 Summer Monsoon, Science, 334, 502-505, https://doi.org/10.1126/science.1204994, 2011.
- 593 Buchard, V., Randles, C., Da Silva, A., Darmenov, A., Colarco, P., Govindaraju, R., Ferrare, R., Hair, J., Beyersdorf,
- 594 A., and Ziemba, L.: The MERRA-2 aerosol reanalysis, 1980 onward. Part II: Evaluation and case studies, J. Climate,
- 595 30, 6851-6872, https://doi.org/10.1175/jcli-d-16-0613.1, 2017.
- 596 Caldwell, P., Chin, H.-N. S., Bader, D. C., and Bala, G.: Evaluation of a WRF dynamical downscaling simulation over
- 597 California, Climatic Change, 95, 499-521, https://doi.org/10.1007/s10584-009-9583-5, 2009.
- 598 Chen, F., Yang, Y., Yu, L., Li, Y., Liu, W., Liu, Y., and Lolli, S.: Distinct effects of fine and coarse aerosols on
- 599 microphysical processes of shallow-precipitation systems in summer over southern China, Atmos. Chem. Phys., 25,
- 600 1587-1601, https://doi.org/10.5194/acp-25-1587-2025, 2025.
- 601 Chen, H., Hsu, P.-C., and Hu, S.: Role of Quasi-Biweekly Cloud-Radiative Feedback in Modulating and Simulating
- Extreme Rainfall Intensity Over Asian Monsoon Regions, Geophys. Res. Lett., 51, e2024GL111671,
- 603 https://doi.org/10.1029/2024GL111671, 2024.
- 604 Chen, G., Yang, J., Bao, Q., and Wang, W.-C.: Intraseasonal responses of the East Asia summer rainfall to anthropogenic
- 605 aerosol climate forcing, Clim. Dynam., 51, 3985-3998, https://doi.org/10.1007/s00382-017-3691-0, 2018.
- 606 Chen, Y., Yang, K., Zhou, D., Qin, J., and Guo, X.: Improving the Noah Land Surface Model in Arid Regions with an
- 607 Appropriate Parameterization of the Thermal Roughness Length, J. Hydrol., 11, 995-1006
- 608 https://doi.org/10.1175/2010JHM1185.1, 2010.
- 609 Chen, M., Shi, W., Xie, P., Silva, V. B. S., Kousky, V. E., Wayne Higgins, R., and Janowiak, J. E.: Assessing objective
- 610 techniques for gauge-based analyses of global daily precipitation, J. Geophys. Res.-Atmos., 113,
- https://doi.org/10.1029/2007JD009132, 2008.
- 612 Choudhury, G., Tyagi, B., Vissa, N. K., Singh, J., Sarangi, C., Tripathi, S. N., and Tesche, M.: Aerosol-enhanced high
- precipitation events near the Himalayan foothills, Atmos. Chem. Phys., 20, 15389-15399
- 614 https://doi.org/10.5194/acp-20-15389-2020, 2020.
- Dave, P., Bhushan, M., and Venkataraman, C.: Aerosols cause intraseasonal short-term suppression of Indian monsoon
- rainfall, Sci. Rep., 7, 17347, https://doi.org/10.1038/s41598-017-17599-1, 2017.





- Debnath, S., Govardhan, G., Saha, S. K., Hazra, A., Pohkrel, S., Jena, C., Kumar, R., and Ghude, S. D.: Impact of dust
- 618 aerosols on the Indian Summer Monsoon Rainfall on intra-seasonal time-scale, Atmos. Environ., 305, 119802,
- 619 https://doi.org/10.1016/j.atmosenv.2023.119802, 2023.
- 620 Duchon, C. E.: Lanczos Filtering in One and Two Dimensions, J. Appl. Meteorol. Clim., 18, 1016-1022,
- 621 https://doi.org/10.1175/1520-0450(1979)018<1016:LFIOAT>2.0.CO;2, 1979.
- 622 Fan, J., Zhang, R., Tao, W.-K., and Mohr, K. I.: Effects of aerosol optical properties on deep convective clouds and
- 623 radiative forcing, J. Geophys. Res.-Atmos., 113, https://doi.org/10.1029/2007JD009257, 2008.
- Fan, J., Rosenfeld, D., Zhang, Y., Giangrande, S. E., Li, Z., Machado, L. A. T., Martin, S. T., Yang, Y., Wang, J., Artaxo,
- 625 P., Barbosa, H. M. J., Braga, R. C., Comstock, J. M., Feng, Z., Gao, W., Gomes, H. B., Mei, F., Pöhlker, C., Pöhlker,
- 626 M. L., Pöschl, U., and de Souza, R. A. F.: Substantial convection and precipitation enhancements by ultrafine aerosol
- 627 particles, Science, 359, 411-418, https://doi.org/10.1126/science.aan8461, 2018.
- Fast, J. D., Gustafson Jr., W. I., Easter, R. C., Zaveri, R. A., Barnard, J. C., Chapman, E. G., Grell, G. A., and Peckham,
- 629 S. E.: Evolution of ozone, particulates, and aerosol direct radiative forcing in the vicinity of Houston using a fully
- 630 coupled meteorology-chemistry-aerosol model, J. Geophys. Res.-Atmos., 111,
- 631 https://doi.org/10.1029/2005JD006721, 2006.
- 632 Gelaro, R., McCarty, W., Suárez, M. J., Todling, R., Molod, A., Takacs, L., Randles, C. A., Darmenov, A., Bosilovich,
- 633 M. G., Reichle, R., Wargan, K., Coy, L., Cullather, R., Draper, C., Akella, S., Buchard, V., Conaty, A., da Silva, A.
- 634 M., Gu, W., Kim, G.-K., Koster, R., Lucchesi, R., Merkova, D., Nielsen, J. E., Partyka, G., Pawson, S., Putman, W.,
- 635 Rienecker, M., Schubert, S. D., Sienkiewicz, M., and Zhao, B.: The Modern-Era Retrospective Analysis for
- Research and Applications, Version 2 (MERRA-2), J. Climate, 30, 5419-5454, https://doi.org/10.1175/JCLI-D-16-
- 637 0758.1, 2017.
- 638 Global Modeling and Assimilation Office (GMAO): MERRA-2 tayg1 2d aer Nx: 2d,1-Hourly, Time-averaged,
- 639 Single-Level, Assimilation, Aerosol Diagnostics V5.12.4, Goddard Earth Sciences Data and Information Services
- 640 Center (GES DISC) [data set], https://doi.org/10.5067/KLICLTZ8EM9D, 2015a.
- 641 Global Modeling and Assimilation Office (GMAO): MERRA-2 tavg1 2d rad Nx: 2d,1-Hourly, Time-Averaged,
- 642 Single-Level, Assimilation, Radiation Diagnostics V5.12.4, Goddard Earth Sciences Data and Information Services
- 643 Center (GES DISC) [data set]. https://doi.org/10.5067/Q9QMY5PBNV1T, 2015b.
- 644 Ginoux, P., Chin, M., Tegen, I., Prospero, J. M., Holben, B., Dubovik, O., and Lin, S.-J.: Sources and distributions of
- dust aerosols simulated with the GOCART model, J. Geophys. Res.-Atmos., 106, 20255-20273,
- https://doi.org/10.1029/2000JD000053, 2001.
- 647 Grell, G. A. and Freitas, S. R.: A scale and aerosol aware stochastic convective parameterization for weather and air
- quality modeling, Atmos. Chem. Phys., 14, 5233-5250, https://doi.org/10.5194/acp-14-5233-2014, 2014.
- 649 Grell, G. A., Peckham, S. E., Schmitz, R., McKeen, S. A., Frost, G., Skamarock, W. C., and Eder, B.: Fully coupled
- 650 "online" chemistry within the WRF model, Atmos. Environ., 39, 6957-6975,
- https://doi.org/10.1016/j.atmosenv.2005.04.027, 2005.





- 652 Guenther, A. B., Jiang, X., Heald, C. L., Sakulyanontvittaya, T., Duhl, T., Emmons, L. K., and Wang, X.: The Model of
- 653 Emissions of Gases and Aerosols from Nature version 2.1 (MEGAN2.1): an extended and updated framework for
- 654 modeling biogenic emissions, Geosci. Model Dev., 5, 1471-1492, https://doi.org/10.5194/gmd-5-1471-2012, 2012.
- 655 Guo, J., Luo, Y., Yang, J., Furtado, K., and Lei, H.: Effects of anthropogenic and sea salt aerosols on a heavy rainfall
- event during the early-summer rainy season over coastal Southern China, Atmos. Res., 265, 105923,
- 657 https://doi.org/10.1016/j.atmosres.2021.105923, 2022.
- 658 Guo, X., Fu, D., Guo, X., and Zhang, C.: A case study of aerosol impacts on summer convective clouds and precipitation
- over northern China, Atmos. Res., 142, 142-157, https://doi.org/10.1016/j.atmosres.2013.10.006, 2014.
- 660 Hazra, A., Goswami, B. N., and Chen, J.-P.: Role of Interactions between Aerosol Radiative Effect, Dynamics, and
- 661 Cloud Microphysics on Transitions of Monsoon Intraseasonal Oscillations, J. Atmos. Sci., 70, 2073-2087,
- https://doi.org/10.1175/JAS-D-12-0179.1, 2013.
- 663 Hersbach, H., Bell, B., Berrisford, P., Hirahara, S., Horányi, A., Muñoz-Sabater, J., Nicolas, J., Peubey, C., Radu, R.,
- 664 Schepers, D., Simmons, A., Soci, C., Abdalla, S., Abellan, X., Balsamo, G., Bechtold, P., Biavati, G., Bidlot, J.,
- 665 Bonavita, M., De Chiara, G., Dahlgren, P., Dee, D., Diamantakis, M., Dragani, R., Flemming, J., Forbes, R., Fuentes,
- M., Geer, A., Haimberger, L., Healy, S., Hogan, R. J., Hólm, E., Janisková, M., Keeley, S., Laloyaux, P., Lopez, P.,
- 667 Lupu, C., Radnoti, G., de Rosnay, P., Rozum, I., Vamborg, F., Villaume, S., and Thépaut, J.-N.: The ERA5 global
- 668 reanalysis, Q. J. Roy. Meteor. Soc., 146, 1999-2049, https://doi.org/10.1002/qj.3803, 2020.
- 669 Hersbach, H., Bell, B., Berrisford, P., Biavati, G., Horányi, A., Muñoz Sabater, J., Nicolas, J., Peubey, C., Radu, R.,
- 670 Rozum, I., Schepers, D., Simmons, A., Soci, C., Dee, D., and Thépaut, J. N.: ERA5 hourly data on pressure levels
- from 1940 to present, Copernicus Climate Change Service (C3S) Climate Data Store (CDS) [data set],
- https://doi.org/10.24381/cds.bd0915c6, 2023.
- 673 Hong, S.-Y., Noh, Y., and Dudhia, J.: A New Vertical Diffusion Package with an Explicit Treatment of Entrainment
- 674 Processes, Mon. Weather Rev., 134, 2318-2341, https://doi.org/10.1175/MWR3199.1, 2006.
- Hsu, P.-C., Lee, J.-Y., and Ha, K.-J.: Influence of boreal summer intraseasonal oscillation on rainfall extremes in
- 676 southern China, Int. J. Climatol, 36, 1403-1412, https://doi.org/10.1002/joc.4433, 2016.
- Huang, X. and Ding, A.: Aerosol as a critical factor causing forecast biases of air temperature in global numerical weather
- 678 prediction models, Sci. Bull., 66, 1917-1924, https://doi.org/10.1016/j.scib.2021.05.009, 2021.
- Huang, R.-J., Zhang, Y., Bozzetti, C., Ho, K.-F., Cao, J.-J., Han, Y., Daellenbach, K. R., Slowik, J. G., Platt, S. M.,
- 680 Canonaco, F., Zotter, P., Wolf, R., Pieber, S. M., Bruns, E. A., Crippa, M., Ciarelli, G., Piazzalunga, A.,
- 681 Schwikowski, M., Abbaszade, G., Schnelle-Kreis, J., Zimmermann, R., An, Z., Szidat, S., Baltensperger, U., Haddad,
- 682 I. E., and Prévôt, A. S. H.: High secondary aerosol contribution to particulate pollution during haze events in China,
- Nature, 514, 218-222, https://doi.org/10.1038/nature13774, 2014.
- Iacono, M. J., Delamere, J. S., Mlawer, E. J., Shephard, M. W., Clough, S. A., and Collins, W. D.: Radiative forcing by
- long-lived greenhouse gases: Calculations with the AER radiative transfer models, J. Geophys. Res.-Atmos., 113,
- 686 https://doi.org/10.1029/2008JD009944, 2008.





- Jia, H., Hasekamp, O., and Quaas, J.: Revisiting Aerosol–Cloud Interactions From Weekly Cycles, Geophys. Res. Lett.,
 51, e2024GL108266, https://doi.org/10.1029/2024GL108266, 2024.
- Koren, I., Kaufman, Y. J., Remer, L. A., and Martins, J. V.: Measurement of the Effect of Amazon Smoke on Inhibition
 of Cloud Formation, Science, 303, 1342-1345, https://doi.org/10.1126/science.1089424, 2004.
- 691 Lee, K. H., Li, Z., Wong, M. S., Xin, J., Wang, Y., Hao, W.-M., and Zhao, F.: Aerosol single scattering albedo estimated
- 692 across China from a combination of ground and satellite measurements, J. Geophys. Res.-Atmos., 112,
- 693 https://doi.org/10.1029/2007JD009077, 2007.
- Levy, R. C., Mattoo, S., Munchak, L. A., Remer, L. A., Sayer, A. M., Patadia, F., and Hsu, N. C.: The Collection 6
- 695 MODIS aerosol products over land and ocean, Atmos. Meas. Tech., 6, 2989-3034, https://doi.org/10.5194/amt-6-
- 696 2989-2013, 2013.
- 697 Li, Z., Niu, F., Fan, J., Liu, Y., Rosenfeld, D., and Ding, Y.: Long-term impacts of aerosols on the vertical development 698 of clouds and precipitation, Nat. Geosci., 4, 888-894, https://doi.org/10.1038/ngeo1313, 2011.
- 699 Li, M., Liu, H., Geng, G., Hong, C., Liu, F., Song, Y., Tong, D., Zheng, B., Cui, H., Man, H., Zhang, Q., and He, K.:
- 700 Anthropogenic emission inventories in China: a review, Natl. Sci. Rev., 4, 834-866,
- 701 https://doi.org/10.1093/nsr/nwx150, 2017a.
- Li, M., Zhang, Q., Kurokawa, J. I., Woo, J. H., He, K., Lu, Z., Ohara, T., Song, Y., Streets, D. G., Carmichael, G. R.,
- 703 Cheng, Y., Hong, C., Huo, H., Jiang, X., Kang, S., Liu, F., Su, H., and Zheng, B.: MIX: a mosaic Asian
- anthropogenic emission inventory under the international collaboration framework of the MICS-Asia and HTAP,
- 705 Atmos. Chem. Phys., 17, 935-963, https://doi.org/10.5194/acp-17-935-2017, 2017b.
- 706 Li, Z., Lau, W. K.-M., Ramanathan, V., Wu, G., Ding, Y., Manoj, M. G., Liu, J., Qian, Y., Li, J., Zhou, T., Fan, J.,
- Rosenfeld, D., Ming, Y., Wang, Y., Huang, J., Wang, B., Xu, X., Lee, S.-S., Cribb, M., Zhang, F., Yang, X., Zhao,
- 708 C., Takemura, T., Wang, K., Xia, X., Yin, Y., Zhang, H., Guo, J., Zhai, P. M., Sugimoto, N., Babu, S. S., and
- 709 Brasseur, G. P.: Aerosol and monsoon climate interactions over Asia, Rev. Geophy., 54, 866-929,
- 710 https://doi.org/10.1002/2015RG000500, 2016.
- Liebmann, B. and Smith, C. A.: Description of a complete (interpolated) outgoing longwave radiation dataset, Bull. Am.
- 712 Meteorol. Soc., 77, 1275-1277, 1996.
- 713 Lin, Z. and Chen, G.: The Role of Anthropogenic Forcings on the Regional Climate of Summertime Diurnal Variations
- over North China, J. Climate, 36, 4491-4509, https://doi.org/10.1175/JCLI-D-22-0498.1, 2023.
- 715 Liu, Z., Ming, Y., Zhao, C., Lau, N. C., Guo, J., Bollasina, M., and Yim, S. H. L.: Contribution of local and remote
- anthropogenic aerosols to a record-breaking torrential rainfall event in Guangdong Province, China, Atmos. Chem.
- 717 Phys., 20, 223-241, https://doi.org/10.5194/acp-20-223-2020, 2020.
- Manoj, M. G., Devara, P. C. S., Safai, P. D., and Goswami, B. N.: Absorbing aerosols facilitate transition of Indian
- 719 monsoon breaks to active spells, Clim. Dynam., 37, 2181-2198, https://doi.org/10.1007/s00382-010-0971-3, 2011.
- 720 Morrison, H., Thompson, G., and Tatarskii, V.: Impact of Cloud Microphysics on the Development of Trailing Stratiform
- Precipitation in a Simulated Squall Line: Comparison of One- and Two-Moment Schemes, Mon. Weather Rev., 137,
- 722 991-1007, https://doi.org/10.1175/2008MWR2556.1, 2009.





- 723 Mudelsee, M.: Bootstrap confidence intervals, in: Climate Time Series Analysis, Atmospheric and Oceanographic
- 724 Sciences Library (Vol. 51), Springer, Cham, Germany, 61-104, https://doi.org/10.1007/978-3-319-04450-7, 2014.
- 725 National Centers for Environmental Prediction (NCEP), National Weather Service (NWS), NOAA, U.S. Department of
- 726 Commerce (DOC): NCEP FNL Operational Model Global Tropospheric Analyses, continuing from July 1999,
- 727 Research Data Archive at the NCEP, Computational and Information Systems Laboratory [data set],
- 728 https://doi.org/10.5065/D6M043C6, 2000.
- 729 National Oceanic and Atmospheric Administration (NOAA): CPC Global Unified Gauge-Based Analysis of Daily
- 730 Precipitation data [data set], https://psl.noaa.gov/data/gridded/data.cpc.globalprecip.html, last access: 27 April
- 731 2025a.
- 732 National Oceanic and Atmospheric Administration (NOAA): NOAA Interpolated Outgoing Longwave Radiation (OLR)
- data [data set], https://psl.noaa.gov/data/gridded/data.olrcdr.interp.html, last access: 27 April 2025b.
- 734 Pahlow, M., Parlange, M. B., and Porté-Agel, F.: On Monin-Obukhov Similarity In The Stable Atmospheric Boundary
- 735 Layer, Bound.-Lay. Meteorol., 99, 225-248, https://doi.org/10.1023/A:1018909000098, 2001.
- 736 Platnick, S., Hubanks, P., Meyer, K., and King, M. D.: MODIS Atmosphere L3 Daily Product, NASA MODIS Adaptive
- 737 Processing System, Goddard Space Flight Center, U.S.A. [data set],
- 738 https://doi.org/10.5067/MODIS/MOD08 M3.061, 2015.
- 739 Platnick, S., Meyer, K. G., King, M. D., Wind, G., Amarasinghe, N., Marchant, B., Arnold, G. T., Zhang, Z., Hubanks,
- 740 P. A., Holz, R. E., Yang, P., Ridgway, W. L., and Riedi, J.: The MODIS Cloud Optical and Microphysical Products:
- 741 Collection 6 Updates and Examples from Terra and Aqua, IEEE T. Geosci. Remote, 55, 502-525,
- 742 https://doi.org/10.1109/TGRS.2016.2610522, 2017.
- 743 Reid, J. S., Lagrosas, N. D., Jonsson, H. H., Reid, E. A., Sessions, W. R., Simpas, J. B., Uy, S. N., Boyd, T. J., Atwood,
- 744 S. A., Blake, D. R., Campbell, J. R., Cliff, S. S., Holben, B. N., Holz, R. E., Hyer, E. J., Lynch, P., Meinardi, S.,
- Posselt, D. J., Richardson, K. A., Salinas, S. V., Smirnov, A., Wang, Q., Yu, L., and Zhang, J.: Observations of the
- 746 temporal variability in aerosol properties and their relationships to meteorology in the summer monsoonal South
- 747 China Sea/East Sea: the scale-dependent role of monsoonal flows, the Madden–Julian Oscillation, tropical cyclones,
- 748 squall lines and cold pools, Atmos. Chem. Phys., 15, 1745-1768, https://doi.org/10.5194/acp-15-1745-2015, 2015.
- 749 Rosenfeld, D., Lohmann, U., Raga, G. B., O'Dowd, C. D., Kulmala, M., Fuzzi, S., Reissell, A., and Andreae, M. O.:
- 750 Flood or Drought: How Do Aerosols Affect Precipitation?, Science, 321, 1309-1313,
- 751 https://doi.org/10.1126/science.1160606, 2008.
- 752 Shao, T., Liu, Y., Wang, R., Zhu, Q., Tan, Z., and Luo, R.: Role of anthropogenic aerosols in affecting different-grade
- 753 precipitation over eastern China: A case study, Sci. Total Environ., 807, 150886,
- 754 https://doi.org/10.1016/j.scitotenv.2021.150886, 2022.
- 755 Shi, H., Xiao, Z., Zhan, X., Ma, H., and Tian, X.: Evaluation of MODIS and two reanalysis aerosol optical depth products
- over AERONET sites, Atmos. Res., 220, 75-80, https://doi.org/10.1016/j.atmosres.2019.01.009, 2019.





- 757 Singh, C., Ganguly, D., and Sharma, P.: Impact of West Asia, Tibetan Plateau and local dust emissions on intra-seasonal
- oscillations of the South Asian monsoon rainfall, Clim. Dynam., 53, 6569-6593, https://doi.org/10.1007/s00382-
- 759 019-04944-5, 2019.
- 760 Stier, P., van den Heever, S. C., Christensen, M. W., Gryspeerdt, E., Dagan, G., Saleeby, S. M., Bollasina, M., Donner,
- L., Emanuel, K., Ekman, A. M. L., Feingold, G., Field, P., Forster, P., Haywood, J., Kahn, R., Koren, I., Kummerow,
- 762 C., L'Ecuyer, T., Lohmann, U., Ming, Y., Myhre, G., Quaas, J., Rosenfeld, D., Samset, B., Seifert, A., Stephens, G.,
- 763 and Tao, W.-K.: Multifaceted aerosol effects on precipitation, Nat. Geosci., 17, 719-732,
- 764 https://doi.org/10.1038/s41561-024-01482-6, 2024.
- Sun, Y. and Zhao, C.: Distinct impacts on precipitation by aerosol radiative effect over three different megacity regions
- 766 of eastern China, Atmos. Chem. Phys., 21, 16555-16574, https://doi.org/10.5194/acp-21-16555-2021, 2021.
- 767 Surendran, S., Ajay Anand, K. V., Ravindran, S., and Rajendran, K.: Exacerbation of Indian Summer Monsoon Breaks
- by the Indirect Effect of Regional Dust Aerosols, Geophys. Res. Lett., 49, e2022GL101106,
- 769 https://doi.org/10.1029/2022GL101106, 2022.
- 770 Tao, W.-K., Chen, J.-P., Li, Z., Wang, C., and Zhang, C.: Impact of aerosols on convective clouds and precipitation,
- 771 Rev. Geophy., 50, https://doi.org/10.1029/2011RG000369, 2012.
- 772 Tian, B., Waliser, D. E., Kahn, R. A., and Wong, S.: Modulation of Atlantic aerosols by the Madden-Julian Oscillation,
- J. Geophys. Res.-Atmos., 116, https://doi.org/10.1029/2010JD015201, 2011.
- 774 Tsinghua University, China Carbon Emission Accounts and Datasets (CEADs) team, Chinese Academy of
- 775 Environmental Planning of the Ministry of Ecology and Environment (CAEP): Multi-resolution Emission Inventory
- for China and MIX-Asia dataset, MEIC Data Platform [data set], http://meicmodel.org.cn/, last access: 27 April
- 777 2025.
- 778 Twomey, S.: The Influence of Pollution on the Shortwave Albedo of Clouds, J. Atmos. Sci., 34, 1149-1152,
- 779 https://doi.org/10.1175/1520-0469(1977)034<1149:TIOPOT>2.0.CO;2, 1977.
- 780 University Corporation for Atmospheric Research (UCAR): WRF Source Codes and Graphics Software Downloads,
- 781 UCAR [code], https://www2.mmm.ucar.edu/wrf/users/download/get_source.html, last access: 27 April 2025a.
- Viniversity Corporation for Atmospheric Research (UCAR): Fire Emission Factors and Emission Inventories, UCAR
- [data set], https://www.acom.ucar.edu/Data/fire/, last access: 27 April 2025b.
- Vinoj, V., Rasch, P. J., Wang, H., Yoon, J.-H., Ma, P.-L., Landu, K., and Singh, B.: Short-term modulation of Indian
- summer monsoon rainfall by West Asian dust, Nat. Geosci., 7, 308-313, https://doi.org/10.1038/ngeo2107, 2014.
- Wang, Y., Wan, Q., Meng, W., Liao, F., Tan, H., and Zhang, R.: Long-term impacts of aerosols on precipitation and
- lightning over the Pearl River Delta megacity area in China, Atmos. Chem. Phys., 11, 12421-12436,
- 788 https://doi.org/10.5194/acp-11-12421-2011, 2011.
- Wang, Z., Xue, L., Liu, J., Ding, K., Lou, S., Ding, A., Wang, J., and Huang, X.: Roles of Atmospheric Aerosols in
- 790 Extreme Meteorological Events: a Systematic Review, Curr. Pollut. Rep., 8, 177-188,
- 791 https://doi.org/10.1007/s40726-022-00216-9, 2022.





- 792 Wei, S., Hsu, P.-C., and Xie, J.: Effects of Intraseasonal Oscillation on Timing and Subseasonal Predictability of Mei-
- 793 yu Onset over the Yangtze River Basin, J. Climate, 37, 2277-2295, https://doi.org/10.1175/JCLI-D-23-0504.1, 2024.
- Wiedinmyer, C., Akagi, S. K., Yokelson, R. J., Emmons, L. K., Al-Saadi, J. A., Orlando, J. J., and Soja, A. J.: The Fire
- 795 INventory from NCAR (FINN): a high resolution global model to estimate the emissions from open burning, Geosci.
- 796 Model Dev., 4, 625-641, https://doi.org/10.5194/gmd-4-625-2011, 2011.
- 797 Xiao, Z., Yu, Y., Miao, Y., Zhu, S., He, H., Wang, Y., and Che, H.: Impact of Aerosols on Convective System Over the
- 798 North China Plain: A Numerical Case Study in Autumn, J. Geophys. Res.-Atmos., 128, e2022JD037465,
- 799 https://doi.org/10.1029/2022JD037465, 2023.
- 800 Xie, J., Hsu, P.-C., Lee, J.-Y., Wang, L., and Turner, A. G.: Tropical intraseasonal oscillations as key driver and source
- of predictability for the 2022 Pakistan record-breaking rainfall event, npj Clim. Atmos. Sci., 7, 256,
- 802 https://doi.org/10.1038/s41612-024-00809-9, 2024.
- 803 Yanai, M., Esbensen, S., and Chu, J.-H.: Determination of Bulk Properties of Tropical Cloud Clusters from Large-Scale
- 804 Heat and Moisture Budgets, J. Atmos. Sci., 30, 611-627, https://doi.org/10.1175/1520-
- 805 0469(1973)030<0611:DOBPOT>2.0.CO;2, 1973.
- 806 Yang, X., Zhou, L., Zhao, C., and Yang, J.: Impact of aerosols on tropical cyclone-induced precipitation over the
- mainland of China, Climatic Change, 148, 173-185, https://doi.org/10.1007/s10584-018-2175-5, 2018.
- Yang, X., Li, Z., Liu, L., Zhou, L., Cribb, M., and Zhang, F.: Distinct weekly cycles of thunderstorms and a potential
- 809 connection with aerosol type in China, Geophys. Res. Lett., 43, 8760-8768, https://doi.org/10.1002/2016GL070375,
- 810 2016.
- Yu, Y. and Ginoux, P.: Assessing the contribution of the ENSO and MJO to Australian dust activity based on satellite-
- and ground-based observations, Atmos. Chem. Phys., 21, 8511-8530, https://doi.org/10.5194/acp-21-8511-2021,
- 813 2021.
- Yun, Y., Zhang, D.-L., Gao, W., Yin, J., Zhao, C., Li, J., Guo, J., and Liu, H.: Spatiotemporal Variations of the Effects
- of Aerosols on Clouds and Precipitation in an Extreme-Rain-Producing MCS in South China, J. Geophys. Res.-
- Atmos., 129, e2023JD040014, https://doi.org/10.1029/2023JD040014, 2024.
- 817 Zaveri, R. A. and Peters, L. K.: A new lumped structure photochemical mechanism for large-scale applications, J.
- Geophys. Res.-Atmos., 104, 30387-30415, https://doi.org/10.1029/1999JD900876, 1999.
- 819 Zaveri, R. A., Easter, R. C., Fast, J. D., and Peters, L. K.: Model for Simulating Aerosol Interactions and Chemistry
- 820 (MOSAIC), J. Geophys. Res.-Atmos., 113, https://doi.org/10.1029/2007JD008782, 2008.
- 821 Zhang, Y., Gao, Y., Guo, L., and Zhang, M.: Numerical analysis of aerosol direct and indirect effects on an extreme
- rainfall event over Beijing in July 2016, Atmos. Res., 264, 105871, https://doi.org/10.1016/j.atmosres.2021.105871,
- 823 2021.
- 824 Zhang, Y., Wen, X. Y., and Jang, C. J.: Simulating chemistry-aerosol-cloud-radiation-climate feedbacks over the
- 825 continental U.S. using the online-coupled Weather Research Forecasting Model with chemistry (WRF/Chem),
- 826 Atmos. Environ., 44, 3568-3582, https://doi.org/10.1016/j.atmosenv.2010.05.056, 2010.

https://doi.org/10.5194/egusphere-2025-2013 Preprint. Discussion started: 4 June 2025 © Author(s) 2025. CC BY 4.0 License.





Zhao, C., Sun, Y., Yang, J., Li, J., Zhou, Y., Yang, Y., Fan, H., and Zhao, X.: Observational evidence and mechanisms of aerosol effects on precipitation, Sci. Bull., 69, 1569-1580, https://doi.org/10.1016/j.scib.2024.03.014, 2024.
Zhou, S., Yang, J., Wang, W. C., Zhao, C., Gong, D., and Shi, P.: An observational study of the effects of aerosols on diurnal variation of heavy rainfall and associated clouds over Beijing–Tianjin–Hebei, Atmos. Chem. Phys., 20, 5211-5229, https://doi.org/10.5194/acp-20-5211-2020, 2020.
Zhu, A., Xu, H., Deng, J., Ma, J., and Hua, S.: Instant and delayed effects of March biomass burning aerosols over the Indochina Peninsula, Atmos. Chem. Phys., 22, 15425-15447, https://doi.org/10.5194/acp-22-15425-2022, 2022.